

Optimal Virtual Model Control for Robotics: Design and Tuning of Passivity-Based Controllers

Daniel Larby, *Student Member, IEEE*, Fulvio Forni, *Senior Member, IEEE*,

Abstract—Passivity-based control is a cornerstone of control theory and an established design approach in robotics. Its strength is based on the passivity theorem, which provides a powerful interconnection framework for robotics. However, the design of passivity-based controllers and their optimal tuning remain challenging. We propose here an intuitive design approach for fully actuated robots, where the control action is determined by a ‘virtual-mechanism’ as in classical virtual model control. The result is a robot whose controlled behavior can be understood in terms of physics. We achieve optimal tuning by applying algorithmic differentiation to ODE simulations of the rigid body dynamics. Overall, this leads to a flexible design and optimization approach: stability is proven by passivity of the virtual mechanism, while performance is obtained by optimization using algorithmic differentiation.

Index Terms—Compliance and Impedance control, Optimization and Optimal Control, Motion Control of Manipulators, Surgical Robotics: Laparoscopy

I. INTRODUCTION

PASSIVITY-based control methods are crucial for designing of stable and reliable robot controllers [1]–[7]. Passivity-based approaches take into account the energy of the robot-controller interconnection (energy shaping) and regulate its dissipation (damping injection) to guarantee stability. The goal is a passive controlled robot that is stable when interacting with other passive devices. The passivity theorem [8], [9] guarantees stability even if both the robot model and the environment are uncertain, as long as they are passive.

A classical example is the ubiquitous proportional derivative (PD) control plus gravity compensation, in joint or end-effector space [10], [11]. The proportional action has the mechanical interpretation of a spring. Combined with gravity compensation, it shapes the potential energy of the controlled robot. The derivative action has the mechanical interpretation of a damper, which has the effect of slowing down the robot motion towards the minimum of the shaped potential energy (stabilization via damping injection). The resulting controlled robot is passive and very reliable. Classical PD control shows how passivity-based design for fully actuated robot manipulators is a relatively ‘easy’ task.

Although passivity-based control is a well-established control approach, in applications few practical designs go beyond PD control and quadratic potentials. Likewise, established methods such as virtual fixtures [12] and impedance controllers too often remain within the comfort of proportional-derivative reaction to the position error. In general, it is difficult

to connect the design of a complex controller with the specific features of the task. In control-theoretic terms, the challenge is finding the relevant task-dependent metric and then optimizing the structure and parameters of the controller for this metric. Picture the design of a controller for a surgical laparoscopic task [13]–[15], where the surgical tool is constrained to pass through a small, but somewhat compliant aperture into the patient’s body. Precise position or force control are insufficient to tackle the complex interaction required by the task. Attacking this through the mathematical derivation of a specific potential energy of passivity-based control appears to fall short. In fact, what kind of ‘energy-shaping’ is best for this task? Even when the controlled impedance of the robot is considered [16], the desired impedance is often chosen heuristically [17]. Pragmatically, the review [18] concludes that efforts are needed “(...) to establish more systematic guidance or methodology on how to specify impedance parameters [such as desired inertia, damping, and stiffness] to reflect the basic dynamic interaction requirements of robotic manipulations raised from customers (...)”.

Our hypothesis is that passivity-based control remains a central design approach in these complex settings. The question is how to explore the space of passivity-based controllers in terms of task-oriented design and optimal tuning. We propose a two-stage approach: first, design the controller as a *virtual mechanism* connected to the robot; second, tune it using *scientific machine-learning* by differentiation of the rigid-body-dynamics through simulations.

The design of controllers as virtual mechanisms is the philosophy of virtual model control [19], [20]. Conceptualizing the controller as a virtual mechanism falls within the framework of control through interconnection [3], [11], [21], [22], but opens the design space to mechanical intuition and the ability to customize the structure of the controller to the specific features of the task. For the case of laparoscopic surgery, we can design a compliant virtual mechanism that connects to the surgical tool, constraining its interaction with soft tissues. An illustration is provided in Fig. 1. This is neither position nor force control. It shows connections with impedance control, but without enforcing a specific desired impedance. The shaping of the energy is not reduced to the manipulation of mathematical terms, but is determined by the geometry and dynamics of the virtual mechanism and by the virtual interconnection with the surgical tool, both driven by mechanical intuition.

Nonlinearities are often seen as problematic dynamics to be removed. However, in a virtual mechanism, a nonlinear spring serves as a tool to stiffen or saturate at different extensions. Nonlinear mechanical linkages become a tool for shaping the kinetic and potential energy of the system intuitively with-

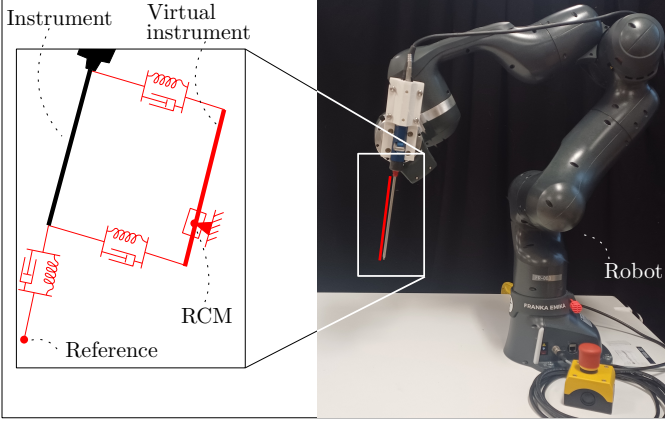


Fig. 1. The virtual mechanism for laparoscopic surgery. The motion of the virtual ‘instrument’, in red, is constrained to a pre-defined remote centre of motion (RCM) through prismatic and rotatory joints. The virtual instrument is ‘attached’ to the robot through springs and dampers. Springs are shown in a stretched configuration, at equilibrium there would be no distance between the virtual instrument and the surgical tool.

out designing custom distance functions for energy-shaping potential fields. Virtual mechanisms are easy to implement using virtual operation space forces. Their implementation is easy to debug, as the controller action can be understood in terms of the physics of the virtual mechanism. If the virtual mechanism is passive, then the closed loop is passive, guaranteeing convergence to a minima of the potential energy of the controlled robot. In fact, the virtual mechanism approach provides robustness for the sim-to-real transition: even with geometric/inertial modeling errors, so long as the robot and controller are passive, we have some level of stability guarantee.

For optimal tuning, we are inspired by recent work on scientific-machine learning: the practise of combining scientific models with gradient-based optimization [23]. Recent developments in automatic differentiation of ordinary differential equation (ODE) solvers have opened the door to efficient optimizations involving continuous-time dynamical systems, attracting increasing attention in robotics [24]–[29]. Scientific machine learning has been used in related applications in physical system identification [30]–[32]; to find optimal state feedback control policies [33]; to perform optimal energy shaping for a pendulum, tuning a controller which is a passive neural network [34]; to design an energy shaping controller to generate desired closed-loop oscillatory trajectories on an undamped double pendulum [35].

In this paper, we embrace this philosophy. We consider the robot as an *open system* whose input/output behavior must be optimized. The optimization of the controller does not rely on general-purpose architectures, such as neural networks, autoencoders, etc. In contrast, our ‘model’ (in the sense of machine learning) is the virtual mechanism designed by the user. The expressivity of the controller, that is, the ability to generate a wide family of control policies, is regulated by the level of parameterization of the virtual mechanism, ranging from stiffness and damping parameters to length, inertia, and other geometrical features of its mechanical linkages.

These parameters are optimized using loss functions that are surrogates of classical performance control metrics, namely the \mathcal{L}_2 and \mathcal{L}_∞ metrics [36]. Compared to [33], the use of virtual mechanisms leads to dynamic feedback policies. Passivity is not enforced through constraints as in [34], but inherited from the structure of the controller.

Computing a gradient through an ODE solver ‘properly’ allows us to compute quickly, thus handle the optimization over the dynamics of the controlled robot efficiently. Using this approach to tune virtual mechanisms can meet the expectations of the review [18] for systematic parameter specification. At the same time, our approach guarantees stability/robustness certificates, which are often missing in state-of-the-art machine learning methods (sim-to-real gap), limiting their applicability in critical domains such as surgical robotics, where a higher level of certainty about controller stability/robustness is required.

The contributions of this paper include: (i) Design of passivity-based controllers as virtual mechanisms, discussed in Sections II and III. These sections extend the early results of [37]. (ii) The adaptation of \mathcal{L}_2 and \mathcal{L}_∞ performance metrics for tractable optimization based on automatic differentiation. This is discussed in Section IV-A. (iii) A tuning approach based on scientific machine learning implemented by algorithmic differentiation of continuous-time simulations, discussed in Section IV-C. This extends the approach of [38], based on linear matrix inequalities [39]. (iv) Simulation results for the 1DOF and 7DOF robot in a surgical setting. We also provide experimental validation, as shown in Section V-B.

II. VIRTUAL MECHANISMS FUNDAMENTALS

A. Virtual forces

To design a controller as a virtual mechanism we need a way to realize the virtual forces arising from the interconnection of virtual mechanism and robot manipulator. These virtual forces must be emulated through the available actuation. Thus, for fully actuated robots, the objective is to drive the actuators of the robot to realise the effect that these virtual forces *would* cause on the dynamics of the robot, using standard methods from Cartesian and operation space control [10], [40], [41]. In what follows, we confine the discussion to virtual forces for reasons of simplicity, but the approach can be extended to include torques.

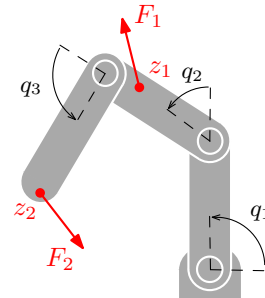


Fig. 2. Virtual forces F_1 and F_2 acting on points z_1 and z_2 .

Consider the robot in Figure 2 with generalized coordinates \mathbf{q} . The generic point \mathbf{z} is a point rigidly attached to one of the robot's links. We want to realize the effect of a virtual force \mathbf{F} at \mathbf{z} . The position of \mathbf{z} in some robot frame (e.g. the robot's base frame) can be represented as a function of the generalized coordinates \mathbf{q} , namely $\mathbf{z} = \mathbf{h}_z(\mathbf{q})$. The velocity reads

$$\dot{\mathbf{z}} = \mathbf{J}_z(\mathbf{q})\dot{\mathbf{q}} \quad (1)$$

where $\mathbf{J}_z(\mathbf{q}) = \frac{\partial \mathbf{h}_z(\mathbf{q})}{\partial \mathbf{q}}$. Both \mathbf{F} and \mathbf{z} are vectors of three elements. By the principle of virtual work [40], the joint actuation

$$\mathbf{u} = \mathbf{J}_z(\mathbf{q})^T \mathbf{F} \quad (2)$$

makes the robot move as if driven by the force \mathbf{F} acting at point \mathbf{z} , where \mathbf{F} is represented in the robot frame of $\dot{\mathbf{z}}$.

The power flow through $(\mathbf{u}, \dot{\mathbf{q}})$ and $(\mathbf{F}, \dot{\mathbf{z}})$ is conserved

$$\mathbf{F}^T \dot{\mathbf{z}} = \mathbf{F}^T \mathbf{J}_z(\mathbf{q}) \dot{\mathbf{q}} = \mathbf{u}^T \dot{\mathbf{q}}. \quad (3)$$

The pairs $(\mathbf{F}, \dot{\mathbf{z}})$ and $(\mathbf{u}, \dot{\mathbf{q}})$ are ports [42] and the Jacobian $\mathbf{J}_z(\mathbf{q})$ models a lossless interconnection between them. The virtual force \mathbf{F} , and its effect on the robot dynamics, are then physically realized via \mathbf{u} .

The effect of multiple virtual forces \mathbf{F}_i at generic points \mathbf{z}_i , $i \in \{1, \dots, n\}$, is captured by superposition [16]:

$$\mathbf{u} = \sum_{i=1}^n \mathbf{J}_{z_i}(\mathbf{q})^T \mathbf{F}_i. \quad (4)$$

B. Virtual elements

The virtual mechanism is built of primitive mechanical elements such as ideal springs, dampers, and inerters combined into virtual structures. Figure 3 shows the symbols adopted in this paper. For simplicity we restrict the discussion to one degree-of-freedom joints, but the approach can be easily extended to more general joints.

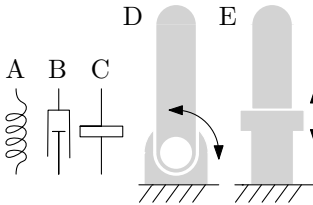


Fig. 3. Components symbols. A) Spring. B) Damper. C) Inerter. D) Revolute joint. E) Prismatic joint.

Springs: An ideal spring is defined by its potential energy function $V : \mathbb{R}^3 \rightarrow \mathbb{R}$, which must be lower bounded for the spring to be passive. Let the displacement $\mathbf{z} = \mathbf{z}_1 - \mathbf{z}_2$ be the extension of a virtual spring whose terminals are connected to the points \mathbf{z}_1 and \mathbf{z}_2 of the robot. The associated forces, \mathbf{F}_1 and \mathbf{F}_2 , respectively acting on \mathbf{z}_1 and \mathbf{z}_2 , are given by the negative gradient of this potential: $\mathbf{F}_1^T = -\frac{\partial V(\mathbf{z})}{\partial \mathbf{z}_1}$ and $\mathbf{F}_2^T = -\frac{\partial V(\mathbf{z})}{\partial \mathbf{z}_2}$. The virtual force of the spring reads

$$\mathbf{F}^T = \frac{\partial V(\mathbf{z})}{\partial \mathbf{z}} \quad (5)$$

and the resulting joint actuation is thus given by

$$\mathbf{u} = -(\mathbf{J}_{z_1}(\mathbf{q}) - \mathbf{J}_{z_2}(\mathbf{q}))^T \mathbf{F}. \quad (6)$$

A linear spring takes $V(\mathbf{z}) = \frac{1}{2}k\mathbf{z}^T\mathbf{z}$, where k is a positive scalar. The corresponding virtual force is $\mathbf{F} = k\mathbf{z}$. Impedance controllers in robotics are often limited to linear springs. However, in applications, it is useful to adopt nonlinear springs, generated by nonquadratic potentials. For example, the potential energy $V(\mathbf{z}) = \frac{\sigma^2}{k} \ln(\cosh(k|\mathbf{z}|/\sigma))$ leads to a virtual force of the form $\mathbf{F} = \sigma \tanh(k|\mathbf{z}|/\sigma) \frac{\mathbf{z}}{|\mathbf{z}|}$. This ‘tanh-spring’ models a useful saturation. In the context of robotic control, this component cannot apply a force greater than σ , which can be used to build mechanisms with a limited maximum force, for safer human-robot interaction. Similarly, the potential energy $k \frac{(\mathbf{z}^T\mathbf{z})^p}{2p}$, $p > 1$, makes the force grow rapidly for $|\mathbf{z}| > 1$, which can be used to enforce constraints on robot motion.

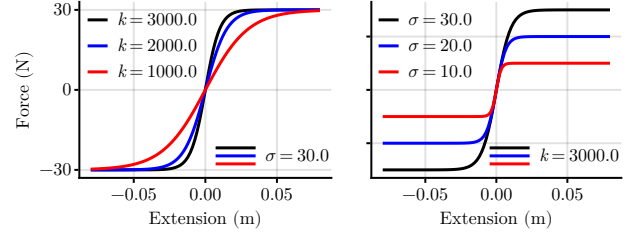


Fig. 4. The nonlinear spring force $\mathbf{F} = \sigma \tanh(k|\mathbf{z}|/\sigma) \frac{\mathbf{z}}{|\mathbf{z}|}$ for different values of the parameters k and σ .

Dampers: Dampers resist motion by dissipating energy. At any instant,

$$\mathbf{F}^T \dot{\mathbf{z}} \geq 0 \quad (7)$$

where \mathbf{F} is the force exerted by the damper at its terminals, as a function of their relative velocity $\dot{\mathbf{z}}$ and their relative displacement \mathbf{z} .

A linear damper satisfies $\mathbf{F} = c\dot{\mathbf{z}}$, where $c \geq 0$ is its damping coefficient. Its braking action removes energy from the system, reducing oscillations. Nonlinear dampers can be very useful for control purposes. Saturating dampers $\mathbf{F} = c \tanh(\dot{\mathbf{z}})$ or localized dampers that are active only in a defined region $\mathbf{F} = c\mu(\mathbf{z})\dot{\mathbf{z}}$, where $0 \leq \mu(\mathbf{z}) \leq 1$, can be used to implement many useful behaviors while remaining within the limits of a passive control action.

Note that the action of a virtual damper on the robot is realized by (6) whenever \mathbf{z} is associated to two generic points on the robot, $\mathbf{z} = \mathbf{z}_1 - \mathbf{z}_2$.

Inerters: The inerter [43] can be considered a generalized inertia/mass. It is used to add inertance to a mechanism. The force of a linear inerter is

$$\mathbf{F} = m\ddot{\mathbf{z}}. \quad (8)$$

where m is the inertance. When one of the terminals is connected to ground, the inerter acts as a point-mass unaffected by gravity.

As virtual springs and dampers, the action of a virtual inerter is realized by (6) whenever \mathbf{z} is associated to two

generic points $z = z_1 - z_2$. In what follows, we avoid attaching virtual inerters to the robot directly, as it is difficult to accurately determine the robot accelerations. We connect inerters to points that are internal to the virtual mechanism that characterize the controller, whose accelerations can be computed analytically. An equivalent choice is often made in many impedance controllers, which shape only the stiffness and damping by leaving the robot's inertia matrix unchanged (the 'target' matrix corresponds to the nominal matrix) [17], [44]–[46].

Remark 1: Like a spring, a nonlinear inverter could be defined using potentials $V : \mathbb{R}^3 \rightarrow \mathbb{R}$ through the relationship

$$\dot{z}^T = \frac{\partial V(x)}{\partial x} \quad \dot{x} = F. \quad (9)$$

where x is an additional 'state' variable. This nonlinear inverter is passive if V is lower bounded. In this form, the inverter is an admittance (force as input and motion as output). The analogy with the spring follows by rewriting (5) as

$$F^T = \frac{\partial V(x)}{\partial x} \quad \dot{x} = \dot{z}. \quad (10)$$

We do not explore nonlinear inerters in this paper to remain within a family of elements that can be easily represented as impedances (motion as input and forces as output).

C. Virtual structures and implementation

Virtual springs, dampers, and inerters are combined into virtual structures defined by a set of rigid bodies connected by rigid and prismatic joints. Extensions to higher-d.o.f. joints are straightforward. Together, these compose the virtual mechanism that represents the controller. The controller has dynamics, since rigid bodies and joints introduce new states. The action of the controller is ultimately determined by the interconnection with the robot, which is always realized through springs and dampers. Figure 5 provides an illustration of the virtual model controller and its interconnection with the robot.

The virtual mechanism is a passive dynamic extension of the robot dynamics (control by interconnection [3]). A virtual mechanism can model mechanical constraints, such as virtual fixtures [12], but its dynamics allow for the modeling of more general dynamical constraints, virtual tools (as shown in Figure 1), and even virtual copies of the robot (digital twin). The geometry of the virtual structure combined with the tuning of the parameters of springs, dampers, and inerters shape the impedance [16] of the interaction port (F_e, z_e) , which captures the response of the robot to the external world.

We endow any virtual structure with mass/inertia/inertance such that its inertia matrix is nonsingular and it can be simulated as a second-order-dynamics. The implementation of the controller is captured in Figure 5. Arrows indicate the flow of information. The robot and the virtual structure act as *admittances*, taking force inputs and returning motion; the interface elements act as *impedances* taking input from motion and returning the forces. To implement the virtual structures, they are simulated in real time, as

$$\ddot{q}_c = M_c(q_c)^{-1}(u_c) \quad (11)$$

where q_c represents the generalized coordinates of the virtual model controller, and M_c is the combined inertia/inertance matrix (the latter due to inerters directly attached to the virtual structure).

The interface elements are formed of spring and dampers, which ultimately depend only upon the position/velocity states of the robot (via the interface coordinates), and do not depend on accelerations.

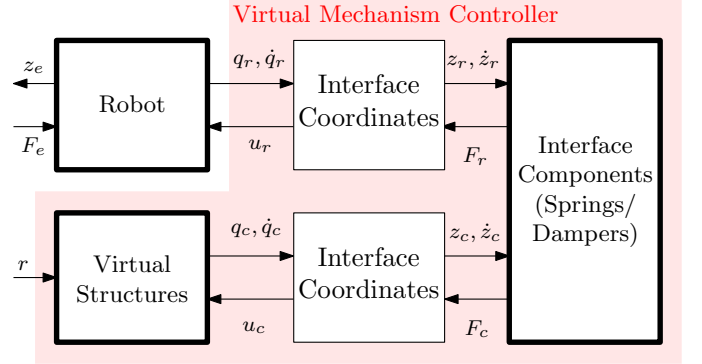


Fig. 5. Virtual model controller block diagram. (F_e, z_e) is an external port. r represent external inputs to the controller.

Remark 2: Constructing the Jacobian is a large part of the computational cost for robots/virtual structures with several joints. Explicit computation of the Jacobian can be avoided for serial robots or tree-structured robots by recursive algorithms, which propagate kinematics/velocities forwards through the structure from the base, and forces backward from the tip(s), while also computing the required joint actuation u . For an example, refer to the backwards pass of the Recursive Newton Euler Algorithm in [47].

Remark 3: Although we limit our discussion to fully actuated robots, virtual model control is still possible for underactuated robots. The mechanism must in that case be designed such that the un-actuated joints are not required to emulate the virtual forces on the robot. Indeed, in Figure 2, the force F_1 does not require any actuation of the third joint. Likewise, in a quadruped, the underactuation is due to the lack of rigid connection to the ground. However, one could design a virtual mechanism acting between any part of the body/legs of the robot [19].

III. THE DESIGN OF VIRTUAL MECHANISMS

A. Virtual model control for reaching

The advantages of designing a controller as a virtual mechanisms can be illustrated by revisiting the classical control of a 'reach' motion, the basic primitive of any manipulator. Once gravity is compensated, the simplest virtual mechanism is given by a virtual spring and a virtual damper connected between the end effector and the target. This corresponds to the classical PD control in the task space [46]. It is straightforward to see that the adoption of nonlinear elements in this context

enables important features. Consider a spring and a damper with nonlinear force-displacement characteristics

$$\mathbf{F}_{\text{spring}} = \sigma_1 \tanh\left(\frac{k|\mathbf{z}|}{\sigma_1}\right) \frac{\mathbf{z}}{|\mathbf{z}|} \quad (12a)$$

$$\mathbf{F}_{\text{damper}} = \sigma_2 \tanh\left(\frac{c|\dot{\mathbf{z}}|}{\sigma_2}\right) \frac{\dot{\mathbf{z}}}{|\dot{\mathbf{z}}|}, \quad (12b)$$

respectively. $\sigma_1 > 0$ and $\sigma_2 > 0$ capture the maximal magnitude of the saturation. In the linear regime of the hyperbolic tangent, $k > 0$ and $c > 0$ are stiffness and damping coefficients. The control action is still passive. The spring has energy $\sigma_1^2 k^{-1} \ln(\cosh(k|\mathbf{z}|/\sigma_1))$, which is lower bounded. The damper dissipates energy with rate $\sigma_2 \tanh(c|\dot{\mathbf{z}}|/\sigma_2)|\dot{\mathbf{z}}|$, which is always positive. In contrast to the linear case, the saturation values σ_1 and σ_2 limit the static force that the end effector exerts on a generic static obstacle. They also limit actuation efforts.

The more advanced exemplary virtual mechanism of Figure 6 allows for refined control over smoothness and peak velocity of the reaching motion. Linear spring and dampers are now attached between the end effector and virtual moving cart. The cart is pulled by a constant force, experiences some drag due to friction, and has mass, which leads to a dynamic controller.

This design has several useful features. It separates the tasks of constraining the robot and driving motion along the line: the spring-damper components between the damper and the cart regulate the constraint, while forces/components applied to the cart regulate the reaching motion. By driving the cart with a constant force rather than as a function of time, we achieve a safer form of path following. Consider an obstruction such as a person in the path of the robot: the end-effector and person collide and the cart continues to move forwards only until equilibrium is reached between the driving force and the constraint-spring. Thus, even for a stiff spring ensuring a strong constraint to the path, we can achieve compliant behaviour along the direction of motion.

The velocity can be regulated by tuning the friction applied to the cart: neglecting the robot's friction, the steady state velocity can be determined by balancing the cart's friction with the applied driving force. Similarly, fast acceleration can be regulated by increasing the inductance of the cart. The cart also has the effect of filtering the driving force: a step change in driving force results in smooth driving torques. For a numerical example of these effects, see Figure 6.

The above considerations illustrate how, in contrast to control synthesis methods based on mathematical derivations, the design of virtual mechanisms carries significant insights on the control action. By relying on physical intuition, we can make predictions about the robot reactions to obstacles, the velocity peak of the end effector, and the filtering effects of the controller dynamics. It is also easier to understand how the parameters of the virtual mechanism will affect the control performance. For example, it is straightforward to imagine that a larger cart mass will induce a stronger lowpass effect on the pulling force, as shown in Figure 6. Similarly, a larger spring stiffness may lead to higher peak forces.

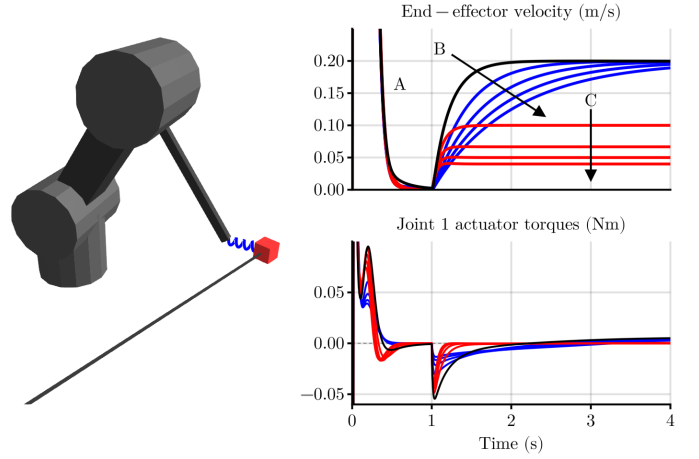


Fig. 6. [Left] Virtual mechanism for reaching. Robot is constrained by a spring damper shown in blue to a virtual cart on a linear rail shown in red. [Right] Simulated end-effector velocity in response to a step input in force (acting on the cart), with varying parameters. A) Initial transients, mostly identical. Nominal response shown in black. B) Varying response for increasing cart mass, blue. Steady state speed does not vary, but acceleration slows. C) Varying response for increasing cart damping, red. Top speed decreases but similar acceleration.

B. Virtual model control for laparoscopic surgery

Virtual model control appears particularly effective on complex tasks. Here we consider robotic surgery, specifically laparoscopic surgery, as shown in Figure 7. The controller has two main objectives: (i) the instrument must pass through a small aperture in the patient's body, often achieved by maintaining the tool over the so-called Remote Center of Motion (RCM), a fixed point in space; (ii) the 'tip' of the instrument must track the reference indicated by the surgeon.

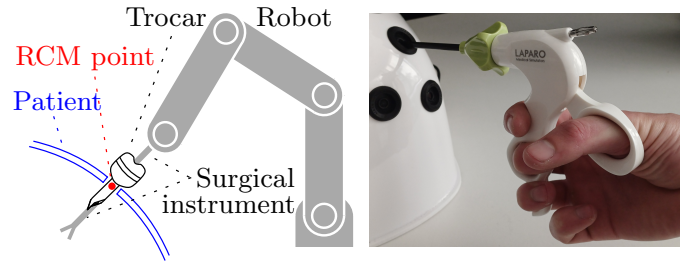


Fig. 7. [Left] Graphical illustration of the main robotic assisted laparoscopic surgery tasks. [Right] Manual laparoscopic instrument and surgical phantom, for comparison.

Figure 1 provides a graphical representation of a virtual mechanism for laparoscopy. After gravity compensation, a 'virtual instrument' is virtually connected to the actual laparoscopic instrument attached to the robot, constraining and driving its motion. It is composed of the virtual instrument itself—a rigid body structure with a spherical joint located at the RCM and a co-located prismatic joint—and a set interface spring-damper pairs. By construction, axis of the virtual instrument always lies on the RCM. The interface springs pull the instrument towards the virtual instrument. At equilibrium, the instrument and the virtual instrument will be

co-located, satisfying the RCM constraint. At the same time, the spring and damper between the end effector at the tip of the instrument and the reference position r will cause the end effector to track the surgeon's motion.

Compared to PD based approaches, our approach does not require inverse kinematics, and therefore gracefully handles redundancy in the robot structure, producing an unconstrained 'null space' (see Figure 8, left). The controller is essentially identical for different robot morphologies. The spring placement allows us to stiffen the robot's behaviour at the RCM independently of the end-effector: compared to energy shaping, the mechanical analogy of the virtual mechanism makes design alterations intuitive, guided by our understanding of the physics of the system. The example on the right of Figure 8 shows the effect of replacing the linear springs between the robot and virtual instrument with saturating springs (described in Figure 4), when faced with a step disturbance force at the port. The saturating spring allows a compliant behaviour at the RCM for large disturbances, while maintaining the constraint for smaller forces. This could be used as an alternative approach to safety at the trocar: failing to a compliant mode rather than a stiff position hold mode, depending on the risk analysis. This design change is enabled by the virtual mechanism analogy.

To implement virtual model controllers no additional sensing beyond torque actuated joints with position/velocity feedback is required, and *dynamic* tuning/filtering can be achieved by changing inertance/damping of virtual instrument. Importantly, because the virtual mechanism is passive, the system is stable for many types of model uncertainty, and external interactions. If the actuators are capable of faithfully producing the desired control forces, then the system is stable regardless of the parameterization of the controller (although in practise there are upper limits on stiffness and damping that can be realized). This helps bridge the sim-to-real gap, as all models are uncertain to a degree, and additionally the system has many unmodified external interactions.

Remark 4: The virtual mechanism presented here is based on the 'Virtual Instrument' of [38], but has a simplified structure. This is due to the tuning method discussed in the next section, which allows for more general virtual mechanisms than [38].

IV. OPTIMAL VIRTUAL MECHANISMS: FORMULATION AND NUMERICAL SOLUTION

A. Input/output performance

Once the virtual mechanism is designed to fulfill the task objectives, its parameters can be adjusted for performance optimization. Despite the intuitive link between design (the mechanism components) and performance (the task), and despite the resilience of the controller to a wide range of parameters and model uncertainties, it is still desirable to fine-tune the performance of the system by considering the response to external disturbances and noise.

In what follow we consider the robot as an open system, as shown in Figure 9. The robot is represented by the upper block, R , and the virtual model controller is represented by

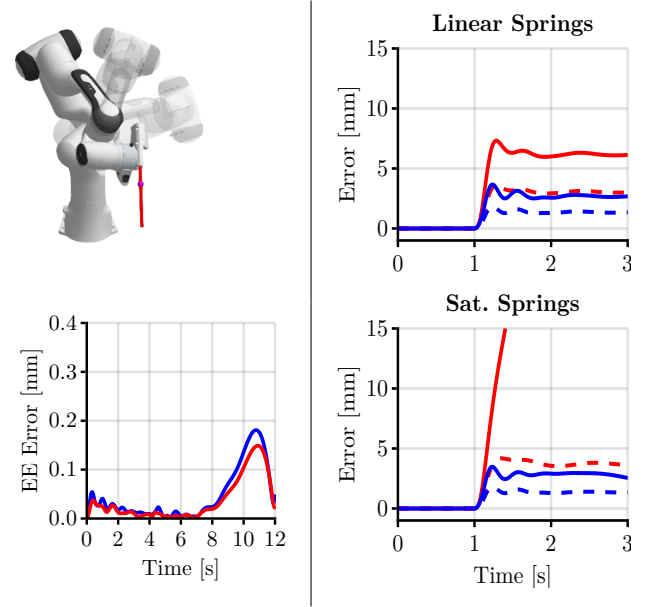


Fig. 8. In each of these figures, red indicates distance from the instrument axis to the RCM, and blue indicates distance from the instrument tip to the reference. [Top-Left] Null space motion: starting pose (solid) and middle/final pose (translucent) for a constant reference/rcm with a 1Nm torque applied at J1 for 12 seconds. [Bottom-Left] End-effector error remains low while moving in the null-space. [Right] Position error at the port and end-effector when a disturbance force is applied at the port. The disturbance force is either 5N (dashed lines) or 10N (solid lines). The top version has linear springs between the virtual-instrument and robot, the bottom has springs that saturate at 5N. We see similar behaviour at the port for smaller forces, but compliant behaviour for a large disturbance. In all cases the end-effector error remains low.

the lower block, C . Performance inputs w model exogenous perturbations to the robot that arise from the interaction with the working environment, such as contact forces. Performance outputs y capture the behavior of interest, that is, displacements and velocities (dynamically weighted) that are relevant to the task. The virtual parameters of the controller are represented by the vector θ , whose elements are greater than or equal to zero, modeling stiffness and damping coefficients, and inertia and geometric parameters such as length and weight of virtual links.

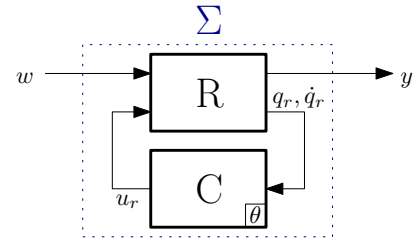


Fig. 9. System Σ from $w \rightarrow y$.

Figure 9 represents a classical setting of linear robust control theory [48], whose objective is to design the controller to guarantee specific closed-loop performance from w to y . In this paper, the controller is restricted to a family of (nonlinear) virtual mechanisms, parameterized by θ , and the goal is to find the parameters θ that optimize a combined \mathcal{L}_2 and \mathcal{L}_∞ performance from w to y . Namely, considering the splitting

of the signals $\mathbf{w} = (\mathbf{w}_1, \mathbf{w}_2)$ and $\mathbf{y} = (\mathbf{y}_1, \mathbf{y}_2)$, we want to optimize the aggregated cost

$$\min_{\boldsymbol{\theta}} \max_{\mathbf{w}} L(\boldsymbol{\theta}, \mathbf{w})$$

$$\text{where } L(\boldsymbol{\theta}, \mathbf{w}) = \frac{\|\mathbf{y}_1\|_2}{\|\mathbf{w}_1\|_2} + \frac{\|\mathbf{y}_2\|_\infty}{\|\mathbf{w}_2\|_\infty} \quad (13)$$

with the standard meaning $\|\mathbf{w}_1\|_2 = (\int_0^\infty \mathbf{w}_1(t)^T \mathbf{w}_1(t) dt)^{\frac{1}{2}}$ and $\|\mathbf{w}_2\|_\infty = \sup_{t \geq 0} |\mathbf{w}_2(t)|$, assuming boundedness of the input signals in their respective domains.

By maximizing over \mathbf{w} , we are looking for the ‘worst’ case, that is, the largest amplification factor from \mathbf{w} to \mathbf{y} (the so-called gain of the system). This can be used to minimize the effect of exogenous disturbances or tracking errors. The ratio between $\|\mathbf{y}_1\|_2$ and $\|\mathbf{w}_1\|_2$ in (13) is based on the *time averages* of the performance signals \mathbf{w}_1 and \mathbf{y}_1 . Therefore, it looks at the long-term effect that a perturbation may have on the robot (this corresponds to the \mathcal{H}_∞ system norm). In contrast, the ratio between $\|\mathbf{y}_2\|_\infty$ and $\|\mathbf{w}_2\|_\infty$ looks at *peaks*, and can be used to analyze short-range phenomena, such as the peak displacement caused by a contact force of given magnitude (this corresponds to the \mathcal{L}_1 system norm). We emphasize that the choice of the relevant input/output pairs $(\mathbf{w}_1, \mathbf{y}_1)$ and $(\mathbf{w}_2, \mathbf{y}_2)$ is going to be determined by the use case.

By optimizing over $\boldsymbol{\theta}$ in (13), we constrain the control action within a predefined set of virtual mechanisms while shaping the response of the controlled robot from \mathbf{w} to \mathbf{y} , i.e. its closed-loop impedance \mathbf{w} to \mathbf{y} . In this sense, (13) extends the classical framework of interconnection and damping assignment [3] to impedance control [16] and performance optimization.

B. Tractable optimization

The min-max form of (13) is a notoriously difficult type of optimization problem [49]. In contrast to linear control theory [48], (13) is far from tractable in the nonlinear and structured setting of virtual mechanisms, as it requires infinitely many probing signals \mathbf{w} . To solve this optimization, we need to build a sequence of approximations that leads to a well-defined, tractable optimization problem. We propose two approaches.

Sampling: select a *finite* family, \mathcal{W} , of perturbing signals \mathbf{w} that are relevant to the engineer. This family could include perturbations that are significant for the specific task or that are known to cause problems. Each sampled signal identifies a *scenario* that the user has identified as relevant. In this case (13) reduces to

$$\min_{\boldsymbol{\theta}} \max_{\mathbf{w} \in \mathcal{W}} L(\boldsymbol{\theta}, \mathbf{w}) \quad (14)$$

Adversarial: alternatively, an adversarial approach could be used to find relevant probing signals that induce poor performance. By maximizing the cost over *parametrized* perturbing signals $\mathbf{w}(\omega)$, where ω is the parameter vector, we can iteratively grow the family of probing signals (scenarios) \mathcal{W}_k , $k \in \mathbb{N}$, by adding those that represent poor operating points of the system. In such a case, the optimization (13) becomes a two-step optimization of the form:

$$\min_{\boldsymbol{\theta}_k} \max_{\mathbf{w} \in \mathcal{W}_k} L(\boldsymbol{\theta}_k, \mathbf{w}) \quad (15a)$$

$$\mathcal{W}_{k+1} = \mathcal{W}_k \cup \{\mathbf{w}(\bar{\omega})\} \text{ for } \bar{\omega} = \operatorname{argmax}_{\omega} L(\boldsymbol{\theta}_k, \mathbf{w}(\omega)) \quad (15b)$$

starting from a given initial \mathcal{W}_0 and iterating over k . Termination could be enforced after a pre-defined number of steps or by considering a bound on the residual improvement.

At the cost of suboptimality, these two approaches simplify the optimization since the inner maximization is now reduced to a finite set of signals (possibly growing). The outer minimization can be solved via gradient descent, as discussed in the next section. Even if suboptimal, Figures 11-13 show that a sufficiently dense set \mathcal{W} for the sampling approach, or a few iteration steps for the adversarial one, provides neat performance results.

C. Solution via algorithmic differentiation

The minimization problem above can be solved by algorithmic differentiation, [24], [50]. The optimal vector $\boldsymbol{\theta}$ can be computed by gradient descent through ODE simulations. We make use of the Julia package *SciMLSensitivity.jl* [23], which integrates with a modular algorithmic differentiation ecosystem in Julia to provide differentiation rules for many ODE solvers in forward and backward modes. In this paper, we use automatic differentiation in the forward mode, which becomes slower to compute the gradient as the number of parameters in $\boldsymbol{\theta}$ scales, but is fast for a small number of parameters and can be used with minimal code adaptation.

A detailed description of automatic differentiation algorithms is beyond the scope of this paper. For parameterized ODE of the form $\dot{\mathbf{x}} = \mathbf{f}(\mathbf{x}, \boldsymbol{\theta})$, we recall that forward automatic differentiation computes the gradient with respect to $\boldsymbol{\theta}$ by solving forward in time the extended system

$$\frac{d}{dt} \begin{bmatrix} \mathbf{x} \\ \frac{\partial \mathbf{x}}{\partial \boldsymbol{\theta}} \end{bmatrix} = \begin{bmatrix} \mathbf{f}(\mathbf{x}, \boldsymbol{\theta}) \\ \frac{\partial \mathbf{f}(\mathbf{x}, \boldsymbol{\theta})}{\partial \mathbf{x}} \frac{\partial \mathbf{x}}{\partial \boldsymbol{\theta}} + \frac{\partial \mathbf{f}(\mathbf{x}, \boldsymbol{\theta})}{\partial \boldsymbol{\theta}} \end{bmatrix}. \quad (16)$$

The gradient of \mathbf{x} at a generic time t is thus obtained by initializing (16) with a suitable selection of $\frac{\partial \mathbf{x}}{\partial \boldsymbol{\theta}}$ at time 0. Thus, to use automatic differentiation, we need to reformulate our optimization problem as a (differentiable) ODE of the form $\dot{\mathbf{x}} = \mathbf{f}(\mathbf{x}, \boldsymbol{\theta})$, possibly paired to some readout function $h(\mathbf{x}(t))$, where h (differentiable) nonlinear mapping of the vector \mathbf{x} at time t . Together, the ODE and the readout function must capture the complete dynamics of the robot and the virtual mechanism. They must also contain additional state variables to compute the aggregate cost L in (13).

Transforming robot and virtual mechanism’s dynamics into a first-order ODE is standard. For the aggregate cost L , we proceed as follows.

- For the \mathcal{L}_2 part, we replace the indefinite integral $\int_0^\infty \dots dt$, with the definite one $\int_0^T \dots dt$, where $[0, T] \subset \mathbb{R}$ is the chosen simulation interval. Then, we compute this integral by introducing two new state variables, $c_{\mathbf{w}_1}$ and $c_{\mathbf{y}_1}$, and the ODE formulation

$$\begin{aligned} \dot{c}_{\mathbf{w}_1} &= \mathbf{w}_1^T \mathbf{w}_1 \\ \dot{c}_{\mathbf{y}_1} &= \mathbf{y}_1^T \mathbf{y}_1 \end{aligned}$$

The value of the \mathcal{L}_2 part of the cost is thus given by $\sqrt{\frac{c_{\mathbf{y}_1}(T)}{c_{\mathbf{w}_1}(T)}}$. In practice, we use $\sqrt{\frac{c_{\mathbf{y}_1}(T)}{\epsilon + c_{\mathbf{w}_1}(T)}}$ to avoid

issues of division by zero due to possible non-zero output transients y_1 for small/zero inputs w_1 , by introducing $\epsilon = 10^{-6}$ in the denominator.

- For the \mathcal{L}_∞ part, we introduce two new states, c_{w_2} and c_{y_2} and we consider the relaxation based on the ODE

$$\begin{aligned}\tau \dot{c}_{w_2} &= \max(c_{w_2}, |w_2|) - c_{w_2} \\ \tau \dot{c}_{y_2} &= \max(c_{y_2}, |y_2|) - c_{y_2}\end{aligned}$$

For sufficiently small time constant $\tau > 0$, $c_{w_2}(T)$ and $c_{y_2}(T)$ tend towards the infinity norm of signals w_2 and y_2 , within the simulation interval $[0, T]$. The value of the \mathcal{L}_∞ part of the cost is thus given by $\frac{c_{y_2}(T)}{c_{w_2}(T)}$. Again, in practice, we use $\frac{c_{y_2}(T)}{\epsilon + c_{w_2}(T)}$.

V. OPTIMAL VIRTUAL MECHANISMS: PERFORMANCE SIGNALS AND PARAMETER TUNING

A. Optimal PD control of a cart

We illustrate the controller optimization on the simplest example of a PD control of a cart. From Figure 10, the equations of cart and controller read

$$m\ddot{q} = u + d \quad (17a)$$

$$u = -k(q + n_q) + b(\dot{q} + n_{\dot{q}}), \quad (17b)$$

where q and \dot{q} are position and velocity of the cart, d is an external force acting on the cart, and n_q and $n_{\dot{q}}$ are disturbances affecting position and velocity measures. m is the mass of the cart and k and b are the proportional and derivative parameters of the controller, which correspond to virtual mechanical stiffness and damping, respectively. These are collected in the parameter vector θ .

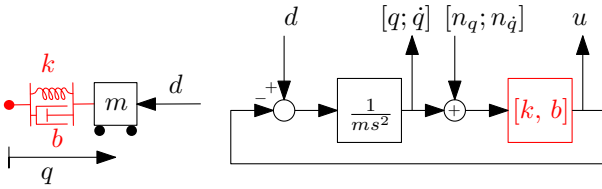


Fig. 10. Illustration of the 1DOF system, with 2 controller parameters and block diagram with exogenous inputs/outputs.

For the optimal tuning, we select the performance input as weighted disturbance and the performance output as a weighted readout of cart position and control force. Namely,

$$\begin{bmatrix} d \\ n_q \\ n_{\dot{q}} \end{bmatrix} = W_w w \quad \text{and} \quad y = W_y \begin{bmatrix} q \\ \dot{q} \\ u \end{bmatrix} \quad (18)$$

where

$$W_w = \begin{bmatrix} 0.01 & 0 & 0 \\ 0 & 0.1 & 0 \\ 0 & 0 & 5 \end{bmatrix} \quad W_y = \begin{bmatrix} 100 & 0 & 0 \\ 0 & 0 & 0 \\ 0 & 0 & 1 \end{bmatrix} \quad (19)$$

are specific (static) weight matrices.

With this selection of the performance pair (w, y) , we can optimize the control parameters to reduce the controlled cart sensitivity to measurement noise and to external forces

acting on it. For instance, by tuning the control parameters to minimize the ratio between y and w , we make the controlled cart less sensitive to these disturbances. The controlled cart will attempt to hold its position even if perturbed by an external force, while mitigating the control effort.

As first case we focus on the \mathcal{L}_2 cost, by setting

$$w_1 = w, \quad y_1 = y, \quad w_2 = 0, \quad y_2 = 0, \quad (20)$$

in (13). We start with the *sampling approach*. We create a set of scenarios \mathcal{W}_N given by sampled sinusoidal signals of increasing frequency

$$\eta_i \sin(\Omega_i t) \quad \text{for } \Omega_i = 0.1 \left(\frac{500}{0.1} \right)^{\frac{i-1}{N-1}} \text{ and } i \in \{1, \dots, N\}, \quad (21)$$

with η_i randomly sampled from the space of 3D unit vectors. Frequencies are sampled exponentially between 0.1rad/s and 500rad/s. The lower frequencies are sampled more densely, as this is where the dynamics of interest occur.

Figure 11 shows a comparison between the true gain \mathcal{L}_2 obtained by H_∞ synthesis [48], and the result of our optimization, as the size of the set of scenarios grows. As a greater number of frequencies are sampled, the cost landscape more closely resembles the ‘true’ cost. The white lines represent the trajectory of the parameters k and b as the optimization converges¹.

Sinusoidal probing is effective here because the controlled cart is a linear system. In general, for nonlinear robots controlled by nonlinear virtual mechanisms we would need a richer sampling space. In practice, we cannot sample infinitely many input signals w , but we can choose them to cover a representative set of scenarios that the robot will face. That is, we can design our probing space in relation to the task. We also observe that, while the cost of the computation scales linearly with the number of sampled signals, the optimization is parallelizable. If required, optimizing over large scenarios can be made feasible by allocating additional computational resources.

The *adversarial approach* provides an alternative to dense sampling, dramatically reducing the number of scenarios. Figure 12 shows the optimization based on the adversarial approach. The two steps of optimization (15a) and (15b) run on scenarios parameterized four elements vectors $\omega^i = [\omega_1^i, \omega_2^i, \omega_3^i, \omega_4^i]^T$, specifically

$$\Omega_i = \omega_1^i \quad \eta^T = [\omega_2^i, \omega_3^i, \omega_4^i], \quad (22)$$

where ω_1^i is sampled in the range $[0, 500]^2$, and $[\omega_2^i, \omega_3^i, \omega_4^i]$ is sampled from the unit normal distribution. An adversarial optimizer is initialized³ and the ‘worst case’ probing signal is obtained by approximating (15b) via 500 iterations (the controller does not change in this phase). Then, the controller adjustment (15a) is resumed. And so on. Figure 12 illustrates the cost function for increasing scenario sizes, starting from

¹We have used the ADAM optimizer with an initial step size of 1.0

²... by taking the exponential of a uniformly sampled parameter in the range $[0, \log(500)]$, so that there is some bias towards lower frequencies.

³An ADAM optimizer with initial step size 2.0

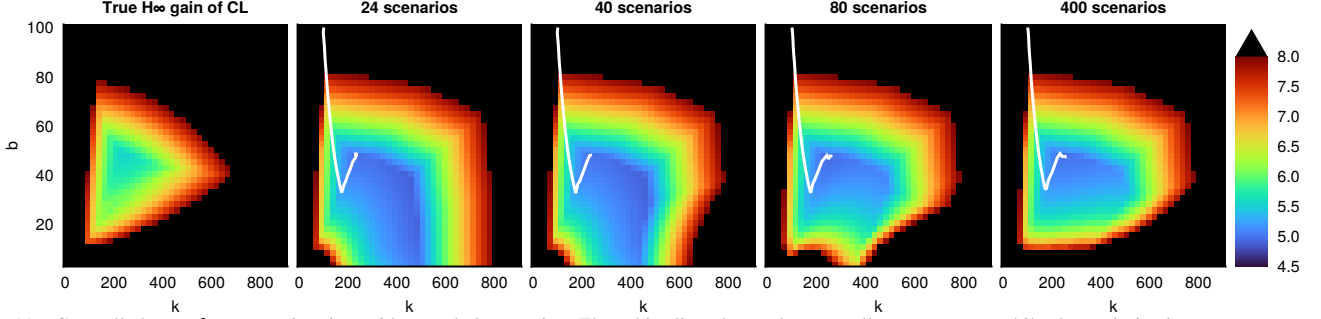


Fig. 11. Controlled cart \mathcal{L}_2 cost estimation with sampled scenarios. The white line shows the controller parameters while the optimization converges.

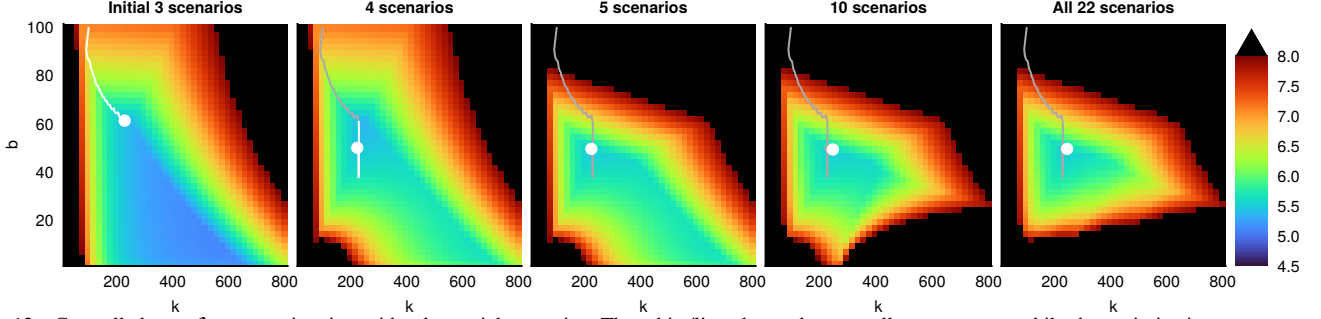


Fig. 12. Controlled cart \mathcal{L}_2 cost estimation with adversarial scenarios. The white/line shows the controller parameters while the optimization converges.

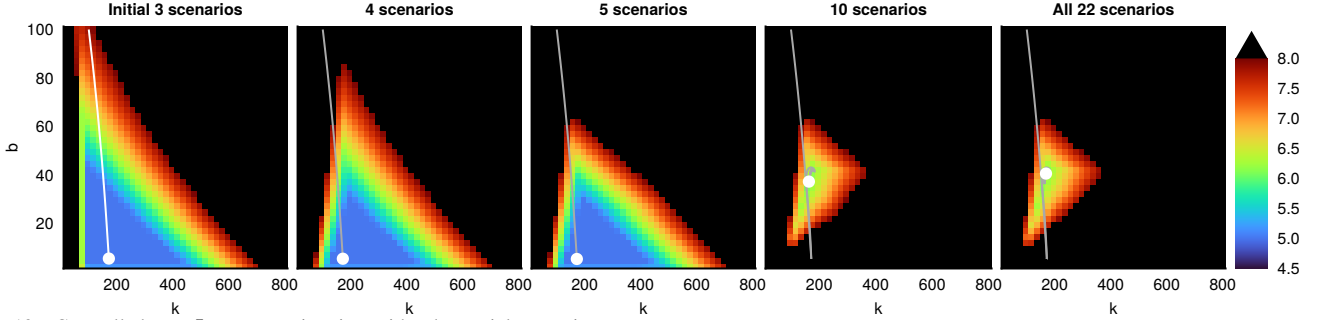


Fig. 13. Controlled cart \mathcal{L}_∞ cost estimation with adversarial scenarios.

a very small setting of three signals. Each new scenario is optimally chosen by (15b).

The summary in Table I and the visual comparison between Figure 12 and Figure 11 show that the adversarial case is in closer agreement with the true cost landscape (top left of Figure 11). Remarkably, this is achieved with only 22 scenarios, a lot less than the 400 scenarios of the sampling case. As the computational cost scales linearly with the number of scenarios, the adversarial approach offers an order-of-magnitude improvement in the tuning time.

	Cost	k	b
True gain	5.5362	237.68	50.0
24 Scenarios	4.9681	231.11	48.51
40 Scenarios	4.9675	230.91	48.56
80 Scenarios	4.9299	259.91	47.61
400 Scenarios	4.9692	254.18	48.26
Adversarial	5.4942	244.24	49.63

TABLE I
CONTROLLED CART PARAMETERS AND ESTIMATED \mathcal{L}_2 COST.

As second case we now consider the \mathcal{L}_∞ cost, by setting

$$w_1 = 0, \quad y_1 = 0, \quad w_2 = w, \quad y_2 = y, \quad (23)$$

in (13). In this case, we use directly adversarial optimization. For simplicity, we use the parameterization (21) as in the \mathcal{L}_2 case, even if sinusoidal signals are not necessarily the best choice to calculate the \mathcal{L}_∞ cost. The results are illustrated in Figure 13, which shows significant similarities and differences compared to the cost landscape of Figure 12. The optimal proportional gain k is smaller, while the derivative gain b remains unchanged between the two cases. In contrast to the \mathcal{L}_2 case, we cannot offer here a comparison with the ‘true’ \mathcal{L}_∞ to \mathcal{L}_∞ gain, as this control synthesis problem is still unsolved, even in the linear setting.

B. Optimal Virtual Model Control for Laparoscopic Surgery

We demonstrate the applicability of the optimization approach to useful robotic systems, which have several degrees of freedom, and a more complex virtual-mechanism controller, by applying the tuning procedure to the virtual instrument controller for surgery described in III-B, with an additional virtual joint damper on J1 and on J4 to arrest null space motion in the simulation/tuning (which features no modelled joint-damping).

The robot manipulator kinematics is that of Franka Emika Research 3. We use the inertial parameters determined in [51]. The virtual instrument is given an inertia of $0.05I \text{ kg m}^2$ and an inductance of 1.0 kg by attaching a linear between its centre and ground⁴. For simplicity, these parameters are set and will not be tuned in this paper. There are 3 virtual springs and 5 virtual dampers to optimize, which leads to a vector of control parameters θ of eight elements.

We focus on the \mathcal{L}_2 norm, adopting again (20). To enforce non-negativity of stiffness and damping parameters, we introduce a nonlinear mapping ϕ between optimization parameters θ and stiffness/damping values $\hat{\theta} = \phi(\theta)$. Specifically, we take $\hat{\theta}_i = \exp(\theta_i)$ if the parameter is a stiffness, and $\hat{\theta}_i = \frac{1}{100} \exp \theta_i$ if the parameter is a damping coefficient. We choose the exponential function as it has no discontinuities and provide a suitable parameter normalization for the optimizer. We also consider the addition of a regularization term

$$\sum_i \max(0, |\theta_i| - 3000)^2 \quad (24)$$

to limit the maximum stiffness and damping values. We penalize components of θ above $\ln(3000)$, as robot actuators cannot realize excessive stiffness / damping. This corresponds to a soft limit on the stiffnesses at 3000 and the damping coefficients at 30.0⁵. The corresponding values pre and post optimization are shown in Table II.

Description	Initial		Final	
	θ	$\hat{\theta}$	θ	$\hat{\theta}$
EE-ref stiffness	6.91	1000	8.02	3056.4
Base-VI stiffness	6.91	1000	7.22	1368.4
EE-VI stiffness	6.91	1000	8.00	2993.7
EE-ref damping	6.91	1000	8.01	30.1
Base-VI damping	6.91	1000	7.86	25.8
EE-VI damping	6.91	1000	7.97	28.8
J1 damping	6.91	1000	3.74	0.421
J4 damping	6.91	1000	6.27	5.29

TABLE II
INITIAL AND TUNED PARAMETERS (ROUNDED)

For the performance input w , we consider several channels. Disturbance forces are applied at two locations: a force d_{ee} is applied at the end effector and a second force d_{rcm} is applied to the instrument at the point closest to the remote centre of motion (RCM). We consider noise n_q and $n_{\dot{q}}$ applied to joint-level measurements of q and \dot{q} , resulting in a 14 dimensional noise vector (for the 7DOF robot). Finally, the surgeon inputs are taken into account through the reference signal r , which provides the desired end-effector displacement. Specifically, the end-effector reference $r_{ee} = r_0 + r$, where r_0 is the initial end-effector position. We consider

$$\begin{bmatrix} d_{ee} \\ d_{rcm} \\ n_q \\ n_{\dot{q}} \\ r \end{bmatrix} = \underbrace{\begin{bmatrix} W_{d_{ee}} & 0 & 0 & 0 & 0 \\ 0 & W_{d_{rcm}} & 0 & 0 & 0 \\ 0 & 0 & W_{n_q} & 0 & 0 \\ 0 & 0 & 0 & W_{n_{\dot{q}}} & 0 \\ 0 & 0 & 0 & 0 & W_r \end{bmatrix}}_{W_w} w, \quad (25)$$

⁴This is equivalent to endowing a point mass of 1 kg in zero gravity.

⁵This is a crude way to avoid reaching the performance limits of our robot. A better identification of the bandwidth limits of the joints is needed to develop a more principled approach, beyond the scope of this paper.

where $W_{d_{ee}} = 8I$, $W_{d_{rcm}} = 4I$, $W_{n_q} = 0.002I$, $W_{n_{\dot{q}}} = 0.1I$, and $W_r = 0.05I$. We assume that the input w is a vector of sinusoids with maximal norm of 1, therefore the disturbance forces peak at 8 N on the end-effector or 4 N on the port, and the reference requires a displacement not larger than 5 cm . Noise on the velocity variables is greater than on the position variables, as velocities are ordinarily obtained by numerical differentiation, which amplifies noise.

The performance output y captures relevant position errors

$$y = Q \begin{bmatrix} x_{ee} - r_{ee} \\ e_{rcm} \end{bmatrix}, \quad (26)$$

where x_{ee} denotes the position of the end effector and e_{rcm} represents the ‘port error’, that is, the minimal displacement between the centre of the port and the longitudinal axis passing through the instrument, as shown in Figure 14. The output weighting matrix is chosen to emphasize performance at the end-effector, for which precision is more important.

$$Q^2 = \begin{bmatrix} I_{3 \times 3} & 0 \\ 0 & 0.2I_{2 \times 2} \end{bmatrix} \quad (27)$$

By minimizing the ratio between $\|w\|_2$ and $\|y\|_2$ we reduce the effect of noise, external disturbances, and reference signals on these position errors, improving accuracy.

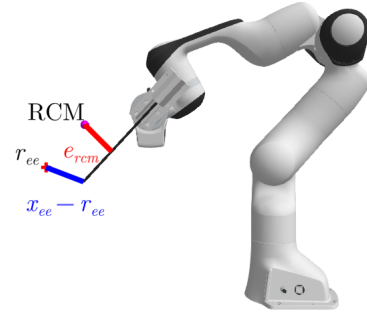


Fig. 14. Performance outputs considered for the optimization of the parameters of the virtual instrument. e_{rcm} is a length 2 vector representing the x/y position of the RCM in the instrument frame. The instrument axis is along the z axis of the instrument frame, thus $\|e_{rcm}\|_2$ is the shortest distance from the instrument axis to the RCM. $x_{ee} - r_{ee}$ is the vector from the reference to the end-effector, and thus $\|x_{ee} - r_{ee}\|_2$ is the distance from the end-effector to the reference.

For the numerical optimization, we initialize the robot simulations at a rest position, with the end effector near the desired position and the instrument passing through the port. We optimise over 7 scenarios, summarized in Table III. Each scenario includes a combination of noise $n = [n_q^T, n_{\dot{q}}^T]^T$, disturbance $d = [d_{ee}^T, d_{rcm}^T]^T$, and reference signal r , which are otherwise zero. We consider

$$n_q = n_{\dot{q}} = [1 \ 1 \ 1 \ 1 \ 1 \ 1]^T \frac{\sin(50t)}{\sqrt{7}} \quad (28a)$$

$$d_{ee} = d_{rcm} = [1 \ 1 \ 1]^T \frac{\sin(2t)}{\sqrt{3}} \quad (28b)$$

$$r = [1 \ 0 \ 0]^T \frac{\sin(3t)}{\sqrt{3}}. \quad (28c)$$

Noise signals act at high frequency. Tracking is probed against slow disturbances and with references at 3 rad/s , under the

assumption that this is the fastest frequency demanded by the surgeon. Good tracking performance at this frequency ensures good tracking at lower frequencies.

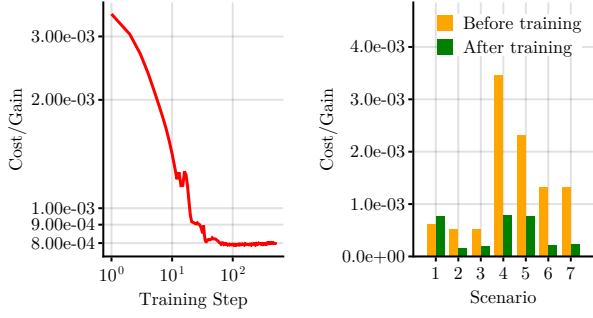


Fig. 15. Training results. [Left] Log-log cost vs training step. [Right] Initial and final costs, $\frac{\|y\|_2}{\|w\|_2}$, on each individual scenario.

	n	d	r
Scenario 1	x		
Scenario 2		x	
Scenario 3	x	x	
Scenario 4			x
Scenario 5	x		x
Scenario 6		x	x
Scenario 7	x	x	x

TABLE III

EXOGENOUS SIGNALS PRESENT IN EACH SCENARIO

We test the optimized parameters on each scenario, as illustrated in Figure 15, right. The exogenous inputs included in each scenario are indicated in Table III, alongside the (rounded) tuned parameters. The comparison between the initial parameters and optimal tuning shows a consistent improvements in the cost metric in response to disturbances and references. The case scenario 1 shows how the optimizing over all scenarios may increase the gain in a specific scenario. Plots of the achieved performance for Scenarios 2 and 4 are shown in Figure 16. These show the resulting decrease in error at the end-effector and at the RCM in response to the pure disturbance and pure reference signals respectively.

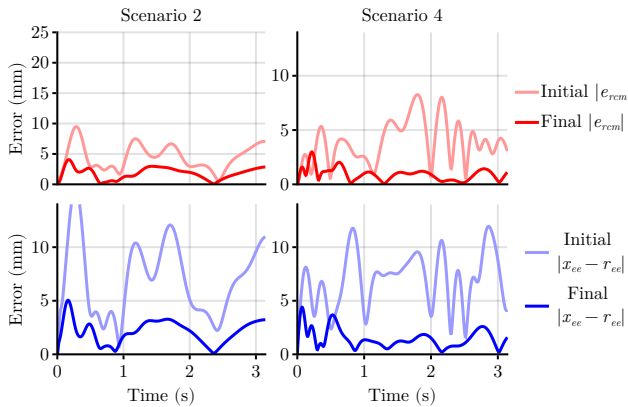


Fig. 16. Comparison before and after optimization for Scenarios 2 and 4.

VI. EXPERIMENTAL VALIDATION

We validate the optimal controller of Section V-B experimentally on a Franka Emika manipulator. The robot is illustrated in Figure 1, and it is tested passing through 4 different ports on the surgical phantom of Figure 7. The RCM location is determined by moving the robot so that the tip of the instrument is at the centre of the port, and measuring the location. Then the robot is moved by hand so that the instrument is inserted into the phantom, and the controller is started. To mimic a surgical reference, we apply a reference signal around the starting tip location of $r = [0.02 \sin(t), 0.01 \sin(2t), 0]^T$, a figure-8 motion in the x/y plane with peak-peak amplitude 40mm, with frequency components at 1rad/s and 2rad/s as shown in Figure 17 D.

The controller runs on a PC that communicates with the robot via a C++ program based on the “libfranka” library. The virtual model controller is written in Julia using the *VM-RobotControl.jl* library⁶, developed by the authors, to simulate the virtual instrument, and compute the desired robot torques due to the interface components. This library is used both for the tuning and implementation of the controller. During the simulation stage, the controller is interfaced with a simulated Franka-Emika robot. At implementation stage, the simulated robot is replaced by the real robot, via rerouting of the communication. The virtual model controller runs on a linux PC with the real-time kernel patch and transmits the desired joint torques to the robot at a rate of 1kHz, which are then realized by the robot’s internal joint torque controllers.

The tip/RCM errors shown in Figure 17 E and F vary depending on the port/pose, but typically remains under 8mm. The RCM error typically remains under 5mm. This reference tracking could potentially be improved by increasing the limit of stiffness; or by the compensation of friction and coriolis/centrifugal forces; or by shaping the inertia matrix of the robot to reduce its apparent inertia. These additional control terms are non-passive, but proven methods if an accurate robot dynamic model is available, and are entirely compatible with the virtual mechanism approach.

Because of our approach and the structure of the controller, particularly its passivity, we expect that the interconnection of the virtual model controller and the real robot should remain stable. This is despite mismatches between the robot model used for the tuning and the robot itself, such as uncertainty in the inertia parameters and the lack of any joint-friction model. Due to the constraint of passing through the ports of the surgical phantom, all of the 4 poses tested, represented in Figure 17 C, deviate from the training pose. This results in a different behaviour to that experienced in simulation and tuning. However, due to the structure of the controller, we still expect reasonable performances. Notably, if the sensing/communication/actuation loop accurately renders the desired torques, the passivity of the controller guarantees that the closed loop system will be stable even if the dynamics of the real robot do not match the simulated dynamics *and* under interaction with external passive systems, such as the

⁶Which can be viewed at <https://github.com/Cambridge-Control-Lab/VMRobotControl.jl>.

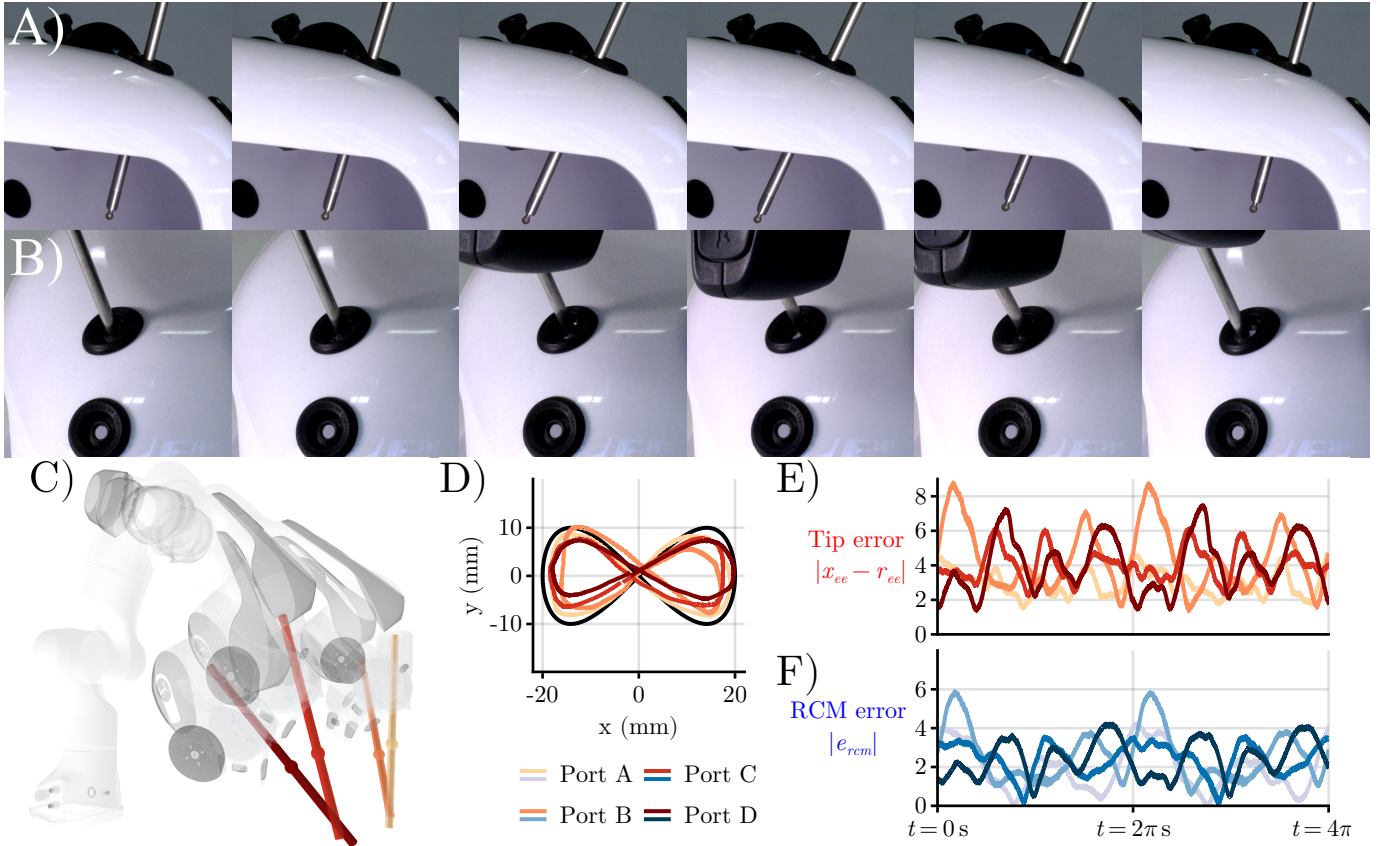


Fig. 17. Experimental performance of the controller while passing through 4 different ports on a laparoscopy training phantom. Video frames showing port A at $t=0$ s, 1 s, \dots 5 s, from the side A) and top B) of the phantom respectively. C) Initial poses for of the robot/virtual instrument. D) Tip error x/y trajectories. E) Tip error magnitude. F) RCM error magnitudes. All positions are computed using the kinematics of the robot and measured joint angles.

interaction between the instrument and the port. However, a loss of performance is expected due the mismatch between ideal and real parameters of the robot.

VII. CONCLUSIONS

We have presented an approach that combines the strengths of virtual-mechanisms with iterative tuning via optimization using automatic differentiation. This approach incorporates nonlinear dynamics, nonlinear controllers and nonlinear cost functions, allowing it to be flexible and general. The approach takes advantage of the chosen control structures to ensure structural properties of the controller, such as passivity. Passivity guarantees closed-loop stability, both in simulations and experiments. This facilitates iterative tuning in simulations, and helps with the sim-to-real transition, despite model uncertainties.

Our approach has two fundamental limitations. One is intrinsic to the non-convexity of the optimization problem (13), leading to local minima and lack of convergence guarantees. However, for the parameterization and cost functions of our examples, we have shown that the optimization converges, recovering classical linear results (Section V-A), and handling the complexity of the Franka-Emika manipulator (Section V-B). The other limitation is the dependence of performance optimization on the accuracy of the robot model, which is challenging, particularly with phenomena such as non-linear

friction dependent on load / temperature [52] and transmission non-linearities [53], [54].

This virtual mechanism approach to passivity-based control shifts design of robot controllers and their parameters into a space familiar to engineers. The design of the controller structure is framed in the language of mechanisms: components, springs, dampers, joints, and links. Within the framework of virtual mechanism controllers there is much to explore: such the multitude of possible components, including the examples of nonlinear springs and dampers given here.

In the limit of highly parameterized and highly numerous components, our approach looks similar to physics-informed neural networks, as seen in [34] where the controller is a passive highly parameterized neural network. The trade-off between the flexibility of the controller for performance optimization and the physical intuition provided by virtual mechanisms can be explored by placing highly parameterized components at specific points on the virtual mechanism. Furthermore, the adoption of highly parameterized structural parts can further improve performance while retaining the physical intuition on the behavior of the controller / virtual mechanism. Future research will focus on these important aspects. We will also look at data-driven tuning to reduce the gap between simulation and experimental performances.

ACKNOWLEDGMENTS

REFERENCES

- [1] M. Takegaki and S. Arimoto, "A New Feedback Method for Dynamic Control of Manipulators," *Journal of Dynamic Systems, Measurement, and Control*, vol. 103, no. 2, pp. 119–125, Jun. 1981.
- [2] R. Ortega, A. J. van der Schaft, I. Mareels, and B. Maschke, "Putting energy back in control," *IEEE Control Systems Magazine*, vol. 21, no. 2, pp. 18–33, 2001.
- [3] R. Ortega, A. van der Schaft, F. Castanos, and A. Astolfi, "Control by Interconnection and Standard Passivity-Based Control of Port-Hamiltonian Systems," *IEEE Transactions on Automatic Control*, vol. 53, no. 11, pp. 2527–2542, Dec. 2008.
- [4] N. Chopra, M. Fujita, R. Ortega, and M. W. Spong, "Passivity-Based Control of Robots: Theory and Examples from the Literature," *IEEE Control Systems Magazine*, vol. 42, no. 2, pp. 63–73, Apr. 2022.
- [5] C. Secchi, S. Stramigioli, and C. Fantuzzi, *Control of Interactive Robotic Interfaces: A Port-Hamiltonian Approach*, ser. Springer Tracts in Advanced Robotics. Berlin: Springer, 2007, no. volume 29.
- [6] J.-J. E. Slotine and W. Li, "On the Adaptive Control of Robot Manipulators," *The International Journal of Robotics Research*, vol. 6, no. 3, pp. 49–59, Sep. 1987.
- [7] R. Ortega and M. W. Spong, "Adaptive motion control of rigid robots: A tutorial," *Automatica*, vol. 25, no. 6, pp. 877–888, 1989.
- [8] A. van der Schaft, *L2-Gain and Passivity Techniques in Nonlinear Control*. Cham: Springer International Publishing, 2017.
- [9] R. Sepulchre, M. Janković, and P. V. Kokotović, *Constructive Nonlinear Control*, ser. Communications and Control Engineering Series. London Berlin Heidelberg: Springer, 1997.
- [10] O. Khatib, "A unified approach for motion and force control of robot manipulators: The operational space formulation," *IEEE Journal on Robotics and Automation*, vol. 3, no. 1, pp. 43–53, Feb. 1987.
- [11] R. Ortega, A. Loria, P. J. Nicklasson, and H. Sira-Ramírez, *Passivity-Based Control of Euler-Lagrange Systems*. London: Springer London, Nov. 1998, vol. 1.
- [12] S. A. Bowyer, B. L. Davies, and F. Rodriguez y Baena, "Active Constraints/Virtual Fixtures: A Survey," *IEEE Transactions on Robotics*, vol. 30, no. 1, pp. 138–157, Feb. 2014.
- [13] H. Su, C. Yang, G. Ferrigno, and E. De Momi, "Improved human-robot collaborative control of redundant robot for teleoperated minimally invasive surgery," *IEEE Robotics and Automation Letters*, vol. 4, no. 2, pp. 1447–1453, 2019.
- [14] M. M. Marinho, B. V. Adorno, K. Harada, K. Deie, A. Deguet, P. Kazanzides, R. H. Taylor, and M. Mitsuishi, "A Unified Framework for the Teleoperation of Surgical Robots in Constrained Workspaces," in *2019 International Conference on Robotics and Automation (ICRA)*. Montreal, QC, Canada: IEEE, May 2019, pp. 2721–2727.
- [15] H. Su, C. Yang, J. Li, Y. Jiang, G. Ferrigno, and E. D. Momi, "Hierarchical Task Impedance Control of a Serial Manipulator for Minimally Invasive Surgery," *Proceedings of the 2020 IEEE International Conference on Human-Machine Systems, ICHMS 2020*, 2020.
- [16] N. Hogan, "Impedance Control: An Approach to Manipulation," in *1984 American Control Conference*, Jun. 1984, pp. 304–313.
- [17] —, "Contact and Physical Interaction," *Annual Review of Control, Robotics, and Autonomous Systems*, vol. 5, no. 1, pp. annurev-control-042920-010933, May 2022.
- [18] P. Song, Y. Yu, and X. Zhang, "A Tutorial Survey and Comparison of Impedance Control on Robotic Manipulation," *Robotica*, vol. 37, no. 5, pp. 801–836, 2019.
- [19] J. E. Pratt, "Virtual Model Control of a Biped Walking Robot," Master's thesis, Massachusetts Institute of Technology, Aug. 1995.
- [20] L. Joly and C. Andriot, "Imposing motion constraints to a force reflecting telerobot through real-time simulation of a virtual mechanism," in *Proceedings of 1995 IEEE International Conference on Robotics and Automation*, vol. 1, May 1995, pp. 357–362 vol.1.
- [21] A. Bloch, N. Leonard, and J. Marsden, "Controlled Lagrangians and the stabilization of mechanical systems. I. The first matching theorem," *IEEE Transactions on Automatic Control*, vol. 45, no. 12, pp. 2253–2270, Dec. 2000.
- [22] R. Ortega and E. García-Canseco, "Interconnection and Damping Assignment Passivity-Based Control: A Survey," *European Journal of Control*, vol. 10, no. 5, pp. 432–450, Jan. 2004.
- [23] C. Rackauckas, Y. Ma, J. Martensen, C. Warner, K. Zubov, R. Supekar, D. Skinner, A. Ramadhan, and A. Edelman, "Universal Differential Equations for Scientific Machine Learning," Nov. 2021.
- [24] C. Rackauckas, A. Edelman, K. Fischer, M. Innes, E. Saba, V. B. Shah, and W. Tebbutt, "Generalized physics-informed learning through language-wide differentiable programming," *MIT web domain*, Nov. 2021.
- [25] S. Kim, W. Ji, S. Deng, Y. Ma, and C. Rackauckas, "Stiff neural ordinary differential equations," *Chaos: An Interdisciplinary Journal of Nonlinear Science*, vol. 31, no. 9, p. 093122, Sep. 2021.
- [26] F. Chen, H. Zhao, D. Li, L. Chen, C. Tan, and H. Ding, "Contact force control and vibration suppression in robotic polishing with a smart end effector," *Robotics and Computer-Integrated Manufacturing*, vol. 57, pp. 391–403, Jun. 2019.
- [27] T. A. Howell, S. L. Cleac'h, J. Brüdigam, J. Z. Kolter, M. Schwager, and Z. Manchester, "Dojo: A Differentiable Physics Engine for Robotics," Mar. 2023.
- [28] M. Giffthaler, M. Neunert, M. Stäuble, M. Frigerio, C. Semini, and J. Buchli, "Automatic Differentiation of Rigid Body Dynamics for Optimal Control and Estimation," *Advanced Robotics*, vol. 31, no. 22, pp. 1225–1237, Nov. 2017.
- [29] M. Giffthaler, M. Neunert, M. Stäuble, and J. Buchli, "The Control Toolbox - An Open-Source C++ Library for Robotics, Optimal and Model Predictive Control," in *2018 IEEE International Conference on Simulation, Modeling, and Programming for Autonomous Robots (SIMPAP)*, May 2018, pp. 123–129.
- [30] M. Raissi, P. Perdikaris, and G. E. Karniadakis, "Physics-informed neural networks: A deep learning framework for solving forward and inverse problems involving nonlinear partial differential equations," *Journal of Computational Physics*, vol. 378, pp. 686–707, Feb. 2019.
- [31] S. Greydanus, M. Dzamba, and J. Yosinski, "Hamiltonian Neural Networks," Sep. 2019.
- [32] S. L. Brunton and J. N. Kutz, *Data-Driven Science and Engineering: Machine Learning, Dynamical Systems, and Control*. Cambridge: Cambridge University Press, 2019.
- [33] I. O. Sandoval, P. Petsagkourakis, and E. A. del Rio-Chanona, "Neural ODEs as Feedback Policies for Nonlinear Optimal Control," Nov. 2022.
- [34] S. Massaroli, M. Poli, F. Califano, J. Park, A. Yamashita, and H. Asama, "Optimal Energy Shaping via Neural Approximators," *SIAM Journal on Applied Dynamical Systems*, vol. 21, no. 3, pp. 2126–2147, Sep. 2022.
- [35] Y. Wotte, S. Dummer, N. Botteghi, C. Brune, S. Stramigioli, and F. Califano, "Discovering Efficient Periodic Behaviours in Mechanical Systems via Neural Approximators," Dec. 2022.
- [36] K. Zhou, J. C. Doyle, and J. C. Doyle, *Essentials of Robust Control*, ser. Prentice Hall International Editions. Upper Saddle River, NJ: Prentice Hall, 1998.
- [37] D. Larby and F. Forni, "A Generalized Approach to Impedance Control Design for Robotic Minimally Invasive Surgery," Dec. 2022.
- [38] —, "A Passivity Preserving H-infinity Synthesis Technique for Robot Control," in *2022 IEEE 61st Conference on Decision and Control (CDC)*, Dec. 2022, pp. 1416–1422.
- [39] S. Boyd, L. El Ghaoui, E. Feron, and V. Balakrishnan, *Linear Matrix Inequalities in System and Control Theory*. Society for Industrial and Applied Mathematics, Jan. 1994.
- [40] M. W. Spong, *Robot Dynamics and Control*, 1st ed. USA: John Wiley & Sons, Inc., 1989.
- [41] B. Siciliano and L. Villani, *Robot Force Control*. Boston, MA: Springer US, 1999.
- [42] A. van der Schaft, "Port-Hamiltonian Modeling for Control," *Annual Review of Control, Robotics, and Autonomous Systems*, vol. 3, no. 1, pp. 393–416, 2020.
- [43] M. Smith, "Synthesis of mechanical networks: The inerter," *IEEE Transactions on Automatic Control*, vol. 47, no. 10, pp. 1648–1662, Oct. 2002.
- [44] G. Averta and N. Hogan, "Enhancing Robot-Environment Physical Interaction via Optimal Impedance Profiles," in *2020 8th IEEE RAS/EMBS International Conference for Biomedical Robotics and Biomechanics (BioRob)*, Nov. 2020, pp. 973–980.
- [45] J. Lachner, F. Allmendinger, S. Stramigioli, and N. Hogan, "Shaping Impedances to Comply With Constrained Task Dynamics," *IEEE Transactions on Robotics*, vol. 38, no. 5, pp. 2750–2767, Oct. 2022.
- [46] D. Lawrence, "Impedance control stability properties in common implementations," in *1988 IEEE International Conference on Robotics and Automation Proceedings*, Apr. 1988, pp. 1185–1190 vol.2.
- [47] R. Featherstone, *Rigid Body Dynamics Algorithms*. Boston, MA: Springer US, 2008.
- [48] K. Zhou, J. C. Doyle, and K. Glover, *Robust and Optimal Control*. Upper Saddle River, NJ: Prentice Hall, 1996.

- [49] Y.-P. Hsieh, P. Mertikopoulos, and V. Cevher, “The Limits of Min-Max Optimization Algorithms: Convergence to Spurious Non-Critical Sets,” *International Conference on Machine Learning*, vol. 38, 2021.
- [50] Y. Ma, V. Dixit, M. J. Innes, X. Guo, and C. Rackauckas, “A Comparison of Automatic Differentiation and Continuous Sensitivity Analysis for Derivatives of Differential Equation Solutions,” in *2021 IEEE High Performance Extreme Computing Conference (HPEC)*. Waltham, MA, USA: IEEE, Sep. 2021, pp. 1–9.
- [51] C. Gaz, M. Cognetti, A. Oliva, P. Robuffo Giordano, and A. De Luca, “Dynamic Identification of the Franka Emika Panda Robot With Retrieval of Feasible Parameters Using Penalty-Based Optimization,” *IEEE Robotics and Automation Letters*, vol. 4, no. 4, pp. 4147–4154, Oct. 2019.
- [52] A. C. Bittencourt and S. Gunnarsson, “Static Friction in a Robot Joint—Modeling and Identification of Load and Temperature Effects,” *Journal of Dynamic Systems, Measurement, and Control*, vol. 134, no. 5, p. 051013, Sep. 2012.
- [53] C. W. Kennedy and J. P. Desai, “Estimation and modeling of the harmonic drive transmission in the Mitsubishi PA-10 robot arm,” 2003.
- [54] D. Ma, S. Yan, Z. Yin, and Y. Yang, “Investigation of the friction behavior of harmonic drive gears at low speed operation,” in *2018 IEEE International Conference on Mechatronics and Automation (ICMA)*. Changchun: IEEE, Aug. 2018, pp. 1382–1388.



Daniel Larby received the MEng degree in control and information engineering in 2020 from the University of Cambridge, UK. He is currently working towards a Ph.D. degree in robotic control with applications in robotic surgery with the control lab in the University of Cambridge, UK.

His research interests include robotics, virtual-mechanism control, passivity based control, impedance control, robotic surgery, and algorithmic differentiation.



Fulvio Forni Fulvio Forni is a Professor of Control Engineering at the University of Cambridge, where he has been a faculty member since October 2015. He earned his PhD from the University of Rome ‘Tor Vergata’ in 2010. Following his doctorate, he conducted postdoctoral research at the University of Liège in Belgium. Forni’s research interests encompass feedback control and robotics. He received the prestigious IEEE CSS George S. Axelby Outstanding Paper Award in 2020. He is a Director of Studies of Newnham College at Cambridge and serves as

a co-investigator for the EPSRC Centre for Doctoral Training in Agrifood Robotics ‘Agriforwards’.